Available online at www.sciencedirect.com
ScienceDirect
Trans. Nonferrous Met. Soc. China 31(2021) 2558−2569
Transactions of Nonferrous Metals Society of China
www.tnmsc.cn

Effect of Ga on microstructure and electrochemical performance of Al−0.4Mg−0.05Sn−0.03Hg alloy as anode for Al−air batteries

Ze-hang ZHUANG[1], Yan FENG[1,2], Chao-qun PENG[1,2], Liu-zhong YANG[1], Meng WANG[1]

1. School of Materials Science and Engineering, Central South University, Changsha 410083, China;
2. Key Laboratory of Electronic Packaging and Advanced Functional Materials, Central South University, Changsha 410083, China

Received 9 September 2020; accepted 30 June 2021

Abstract: The effects of 0.01 wt.% Ga on microstructure and electrochemical performance of Al−0.4Mg−0.05Sn−0.03Hg anodes in NaOH solutions were investigated. Potentiodynamic polarization, electrochemical impedance spectroscopy, and galvanostatic discharge tests were used to assess the electrochemical performance of the Al−Mg−Sn−Hg−Ga anodes. The results show that the addition of 0.01 wt.% Ga in Al−0.4Mg−0.05Sn−0.03Hg anode enhances its corrosion resistance and discharge activity. It is benefited from the refined second phases and homogenous microstructure of Al−Mg−Sn−Hg−Ga anode, which restrains the local crystallographic corrosion and chunk effect. Compared with Al−Mg−Sn−Hg anode, the corrosion current density and the mass loss rate of Al−Mg−Sn−Hg−Ga anode decrease by 57% and 93%, respectively. When discharging at the current density of 20 mA/cm^2, the discharge voltage, current efficiency and specific capacity of the single Al−air battery with Al−0.4Mg−0.05Sn−0.03Hg−0.01Ga anode are 1.46 V, 33.1%, and 1019.2 A·h·kg^{-1}, respectively. The activation mechanism of Ga on Al−Mg−Sn−Hg−Ga anode materials was also discussed.

Key words: aluminum alloy; electrochemistry; corrosion; Al−air battery

1 Introduction

With unique and desirable properties such as negative standard electrode potential (−1.66 V vs NHE) and high energetic capacity (2980 A·h·kg^{-1}), aluminum is considered to be one of the most popular anode materials for metal fuel cells [1−3], which hold promise for the next-generation energy storage technologies [4−7]. However, aluminum fuel cells are not as popular as zinc fuel cells by far as protective oxide film is formed spontaneously on the anode surface in the neutral electrolyte, which slows down the active dissolution of metal anode. The severe self-corrosion of aluminum anode in alkaline electrolyte also causes low current efficiency during standby, which limits the commercial use of the aluminum fuel cells [8−10].

Doping Al anode materials with trace alloying elements is believed to be an effective way to reduce self-corrosion and enhance discharge performances [11−14]. The appropriate amount of Mg can improve the electrochemical activity and accelerate the self-corrosion rate of Al alloys in NaOH solution [15]. Hg can accelerate the activation of the Al matrix and control self-corrosion caused by Mg [16]. The second phases containing Mg and Sn in Al alloys promote pitting corrosion and anodic dissolution. The addition of alloying elements such as Mg, Ga, Hg and Zn in Al alloys can shift the potential towards more negative values, causing the activation dissolution of Al [17−22]. Meanwhile, Al−Mg−Sn−Hg alloy has been reported as a promising anode

Corresponding author: Meng WANG, E-mail: 173101005@csu.edu.cn
DOI: 10.1016/S1003-6326(21)65675-3

material to be studied due to its negative electrode potential and high electrochemical activity [16]. Alloying elements such as Pb, Hg, Zn and Sn with high hydrogen over-potential can reduce the cathodic hydrogen evolution reaction of aluminum anode [23,24]. Ga is an attractive alloying element that can activate the surface of aluminum by causing thinning of the passive oxide film where Ga is placed [25]. NESTORIDI et al [26] surveyed the potential shift from −800 to −1500 mV when both Ga and Sn were added to the aluminum anodes in brine medium at room temperature.

In this work, Al−0.4Mg−0.05Sn−0.03Hg and Al−0.4Mg−0.05Sn−0.03Hg−0.01Ga alloys were prepared as anode material for the Al−air battery. Their microstructure and electrochemical performances in 4 mol/L NaOH solution are investigated. The effects of Ga on discharge properties of the Al−0.4Mg−0.05Sn−0.03Hg alloy were discussed.

2 Experimental

2.1 Materials preparation

The nominal compositions of Al−Mg−Sn−Hg and Al−Mg−Sn−Hg−Ga alloys were Al−0.4wt.%Mg−0.05wt.%Sn−0.03wt.%Hg (Alloy 1) and Al−0.4wt.%Mg−0.05wt.%Sn−0.03wt.%Hg−0.01wt.%Ga (Alloy 2), respectively. Two alloys were prepared by melting the ingots of pure Al (99.99 wt.%), pure Mg (99.99 wt.%), pure Sn (99.99 wt.%), Al−10wt.%Ga and Mg−20wt.%Hg master alloy in a graphite crucible in an induction furnace at 750 °C. The molten alloy was then poured into a water-cooled steel mold and cooled down to room temperature. Heat treatment of the specimens was carried out at 350 °C for 30 min. The as-cast alloy ingots were then rolled to the sheets with a thickness of 0.5 mm at room temperature. At last, the rolled alloys were annealed at 300 °C for 2 h. The chemical composition of two alloys was measured by inductively coupled plasma emission spectroscopy (ICP). The results are listed in Table 1. To investigate the morphology of specimens, Quanta-200 scanning electron microscopy (SEM) equipped with energy dispersive spectroscopy (EDS) and JXA−8230 electron probe microanalyzer (EPMA) were used. The phases of prepared samples were identified using an X-ray diffractometer (XRD; D/Max 2500) supplied by Cu K_α radiation. The scanning range of 2θ was from 10° to 80° with a scan step of 8 (°)/min.

Table 1 Actual chemical compositions detected by ICP-OES (wt.%)

Alloy	Mg	Sn	Hg	Ga	Al
1	0.407	0.050	0.033	−	Bal.
2	0.410	0.052	0.031	0.010	Bal.

2.2 Determination of self-corrosion rates

The samples were encapsulated in epoxy resin to expose only a flat working surface (10 mm × 10 mm), ground with abrasive paper and then cleaned with doubly distilled water, dehydrated using ethanol, and dried with a hairdryer. The samples were immersed in 4 mol/L NaOH solution for 150 min to estimate the corrosion rate. The mass of the samples before and after immersion was measured after cleaning the corrosion products formed on sample surface. The corrosion products were cleaned out in solutions of 2% CrO_3 + 5% H_3PO_4 for about 5 min, then rinsed with distilled water and ethanol, and dried by hot airflow.

The mass loss rate (Δm) was calculated using the equation:

$$\Delta m=(m_0-m_1)/(S\cdot t) \quad (1)$$

where m_0 is the initial mass before immersion, m_1 is the final mass after immersion, S is the surface area, and t is the time.

The mass loss rate can be converted to an average corrosion rate (P_w) using the equation [27]:

$$P_w=87.6\Delta m/\rho \quad (2)$$

where ρ is the metal density.

2.3 Electrochemical measurement

A CHI660D electrochemistry workstation equipped with a classical three-electrode cell was adopted to measure the polarization curves and electrochemical impedance spectra (EIS) of all specimens. Each of them was sealed with epoxy resin except for an exposed surface of 10 mm × 10 mm. A saturated calomel electrode (SCE) was served as a reference electrode, a Pt sheet was used as the counter electrode, and the specimen acted as the working electrode. The working surface was ground with SiC abrasive paper from 400 to 1200 grit. All measurements were carried out in 4 mol/L NaOH solution at room temperature ((25±2) °C).

The potentiodynamic polarization curves were measured at a scanning rate of 5 mV/s. The electrochemical impedance spectrum measurements with perturbation amplitude of 10 mV were conducted at open-circuit-potential (OCP) over a frequency range from 100 kHz to 0.01Hz.

2.4 Battery performance test

The performances of Al-air batteries were studied via galvanostatic discharge at 10 and 20 mA/cm^2 for 1200 s using the LAND test system. The electrolyte was 4 mol/L NaOH solution; Alloy 1 and Alloy 2 were used as the anodes and the air cathode was a commercial gas diffusion electrode with MnO_2 catalyst. The anodic efficiency (η) was calculated using the following equation [28]:

$$\eta=9.0I\cdot t/(m'\cdot F) \tag{3}$$

where I is the discharge current, m' is the mass loss after discharge, and F is the Faraday constant. The surface morphology of the anodes after discharge was observed with the SEM (Quanta−200) using the secondary electron (SE) image. To obtain good reproducibility of the data, all electrochemical measurements and battery tests were conducted in triplicate under the same conditions [29].

3 Results and discussion

3.1 Microstructure

The SEM images in Fig. 1 present the morphologies of Alloy 1 and Alloy 2. With the addition of 0.01 wt.% Ga, the amount and size of the second phases decrease. The lump and granular second phases distribute non-homogeneously in Alloy 1, and some lump phases are crushed in the local area. Banded structures along the rolling direction can be observed. In comparison, elongated and less crushed second phases with smaller size occur in Alloy 2, showing relatively homogeneous microstructure.

Since there are no intermetallic compounds in Al−Sn and Al−Hg alloys according to their binary diagrams [30], the second phase particles with more Sn and Hg contents are expected. The element contents of different phases in Fig. 1 determined by

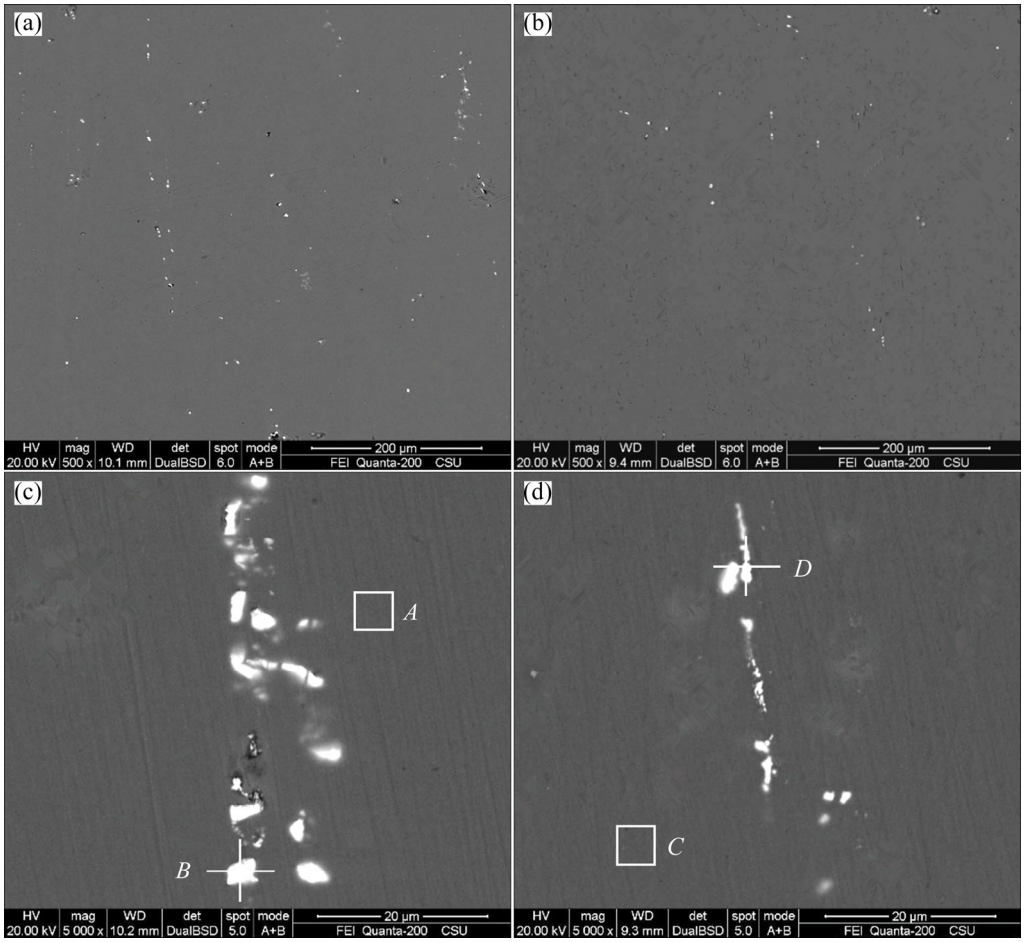

Fig. 1 SEM images of alloys: (a, c) Alloy 1; (b, d) Alloy 2

EPMA are given in Table 2 and the alloying element distributions in Alloy 2 are shown in Fig. 2. The second phases mainly contain Mg, Hg and Sn elements in these two alloys. With the addition of Ga, the contents of Mg in the second phases increase from 17.31% to 25.06%, the contents of Sn increase from 6.18% to 14.66%, while the contents of Hg decrease dramatically from 10.23% to 2.55%. This implies that the addition of Ga promotes the distribution of Mg and Sn in the second phases, while decreases the content of Hg in the second phases. On the contrary, Hg has a solid solution of 0.23% in the Al matrix in Alloy 2, which indicates that the addition of Ga promotes the homogeneous distribution of Hg. The content of Ga in the Al matrix is 0.25 wt.%, close to 0.16 wt.% in the second phases. It can be inferred that Ga elements uniformly distribute in the matrix and the second phase in Alloy 2. The above results are confirmed in Fig. 2, where Mg and Sn are enriched in the second phases, and Hg and Ga distribute relatively uniformly in Alloy 2. The different distributions of alloying elements in the Al matrix and second phases play a vital role in the activation of the anodes. Hg and Ga have a relatively low melting point. The low-melting-point elements present liquid states and show excellent fluidity at the operating temperature of the Al−air batteries. Thus, they can destroy and separate the continuous distribution of the oxide film on the Al anode surface, which indicates enhanced electrochemical performance [31−33].

Table 2 Element contents of different phases in Al alloys identified by EPMA (at.%)

Alloy	Point	Al	Mg	Sn	Hg	Ga
1	*A*	98.73	1.27	–	–	–
	B	66.28	17.31	6.18	10.23	–
2	*C*	97.84	1.68	–	0.23	0.25
	D	57.57	25.06	14.66	2.55	0.16

3.2 Polarization behavior

The potentiodynamic polarization curves of the samples are shown in Fig. 3. It can be observed that the alloys remain active over whole potential range. The anodic and cathodic branches of the alloys are not symmetrical, and cathodic branches

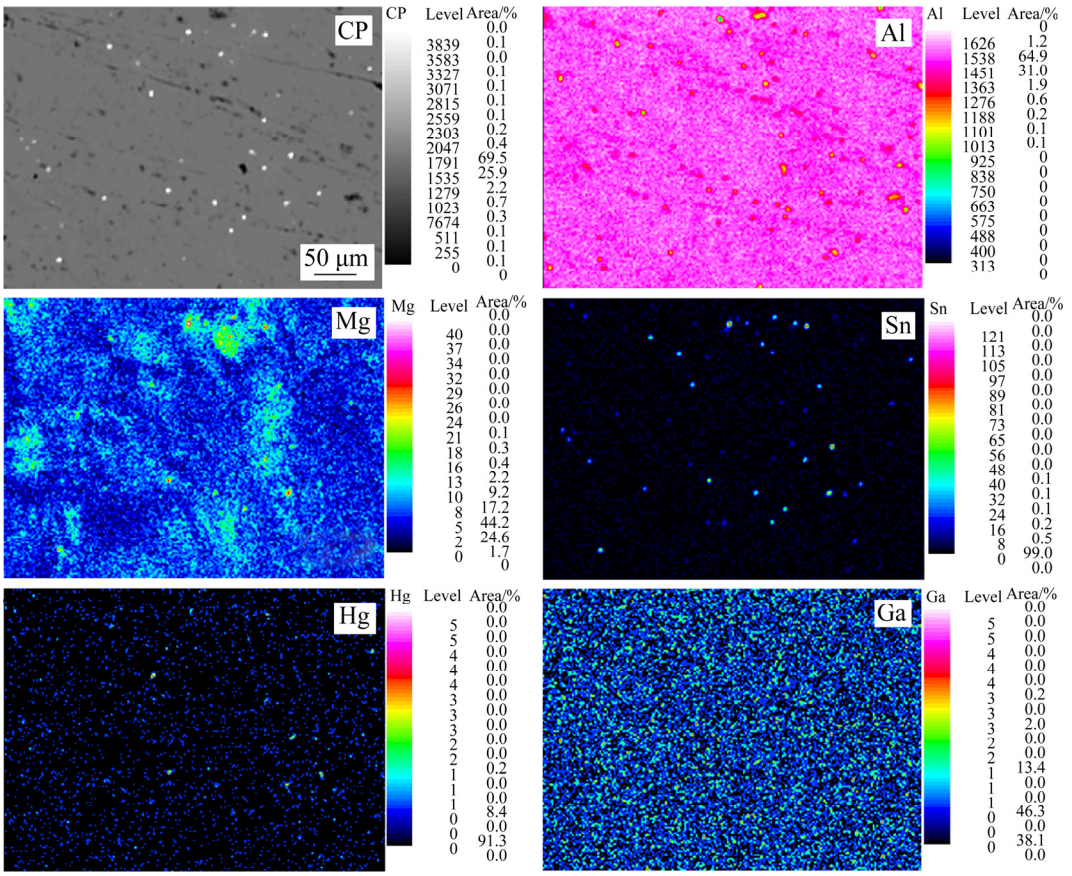

Fig. 2 Distributions of alloying elements in Alloy 2

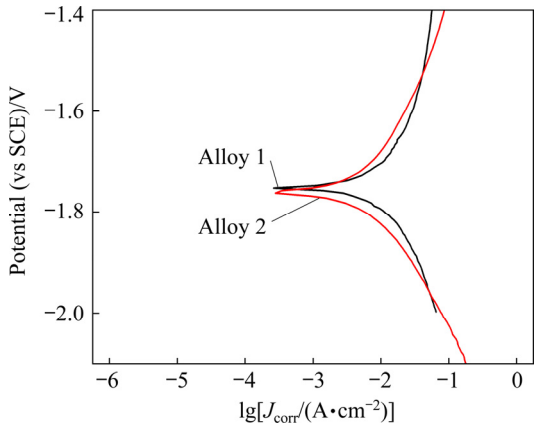

Fig. 3 Polarization curves of alloys in 4 mol/L NaOH solution

exhibit good linearity. Thus, the corrosion current densities are obtained by Tafel extrapolation [34,35]. The calculated corrosion potential (φ_{corr}) and corrosion current density (J_{corr}) of the specimens are listed in Table 3. The corrosion current density is converted into thickness loss rate (P_i) using the following equation:

$$P_i = 87600 J_{corr} \cdot M / (\rho n F) \quad (4)$$

where M is the average molar mass, and n is the mean effective ion charge.

The corrosion potentials of Alloy 1 and Alloy 2 are both approximately −1.76 V. Generally, the corrosion potential of Al alloys in alkalinity solutions is complex, including the oxidation of aluminum, the reduction of water, and the growth of aluminum hydroxide layer, which reflects the corrosion tendency of aluminum to some extent. The reactions are as follows [34,36]:

$$Al + 3OH^- \rightarrow Al(OH)_3\downarrow + 3e \quad (5)$$

$$2H_2O + 2e \rightarrow H_2 + 2OH^- \quad (6)$$

$$Al(OH)_3 + OH^- \rightarrow Al(OH)_4^- \quad (7)$$

Although having similar corrosion potential, the two alloys show a noteworthy difference in corrosion resistance. Compared with Alloy 1, the corrosion current density of Alloy 2 decreases by 57% from 14.12 to 6.05 mA/cm^2. The better corrosion resistance of Alloy 2 is closely related to its microstructure. The second phases, containing activation elements of Sn, Hg and Ga, express cathodic properties in corrosion galvanic cells with an aluminum matrix. As shown in Fig. 1, with the addition of Ga, less amount and smaller size cathodic second phases improve the corrosion resistance.

According to Table 3, with the addition of 0.01 wt.% Ga, mass loss rate decreases significantly by 93% from 39.06 to 2.48 mg·cm^{-2}·h^{-1}. This indicates that the element Ga greatly improves the corrosion resistance. It is consistent with the polarization curves. In addition, the mass loss rate of Alloy 2 is apparently lower than that of the reported ones (Al−1Mg−1Zn−0.1Ga−0.1Sn: 5.69 mg·cm^{-2}·h^{-1} and Al−1Mg−0.1Ga−0.1Sn: 13.19 mg·cm^{-2}·h^{-1} [34]).

The corrosion rates deduced from current corrosion density and mass loss rate (P_i and P_w) are also listed in Table 3. Apparently, two corrosion rates of an alloy are different, and P_w is larger than P_i. The results may be due to the side reactions during the immersion test, which results in higher corrosion rates. At open circuit potential, the main corrosion type of Al alloy is self-corrosion due to the electric negativity difference. However, in polarization curves test, the corrosion current density is calculated from the Tafel equation. The strong polarization status with a constant scanning rate in polarization tests restrains other side corrosion reactions, leading to less P_i than P_w.

3.3 Corrosion morphology

The corrosion morphologies of Alloy 1 and Alloy 2 after immersion in 4 mol/L NaOH solution for 150 min with and without the corrosion products are shown in Fig. 4. From Fig. 4(a), the corrosion product on the surface of Alloy 1 is

Table 3 Corrosion parameters of different anode materials in 4 mol/L NaOH solution

Sample	φ_{corr} (vs SCE)/V	J_{corr}/(mA·cm^{-2})	P_i/(mm·a^{-1})	Mass loss rate/(mg·cm^{-2}·h^{-1})	P_w/(mm·a^{-1})
Alloy 1	−1.75	14.12	153.86	39.06	1268.45
Alloy 2	−1.76	6.05	65.92	2.48	80.54
Al−1Mg−0.1Ga−0.1Sn [36]	−1.70	6.75	73.75	13.19	429.50
Al−1Mg−1Zn−0.1Ga−0.1Sn [36]	−1.76	6.17	67.00	5.69	184.15

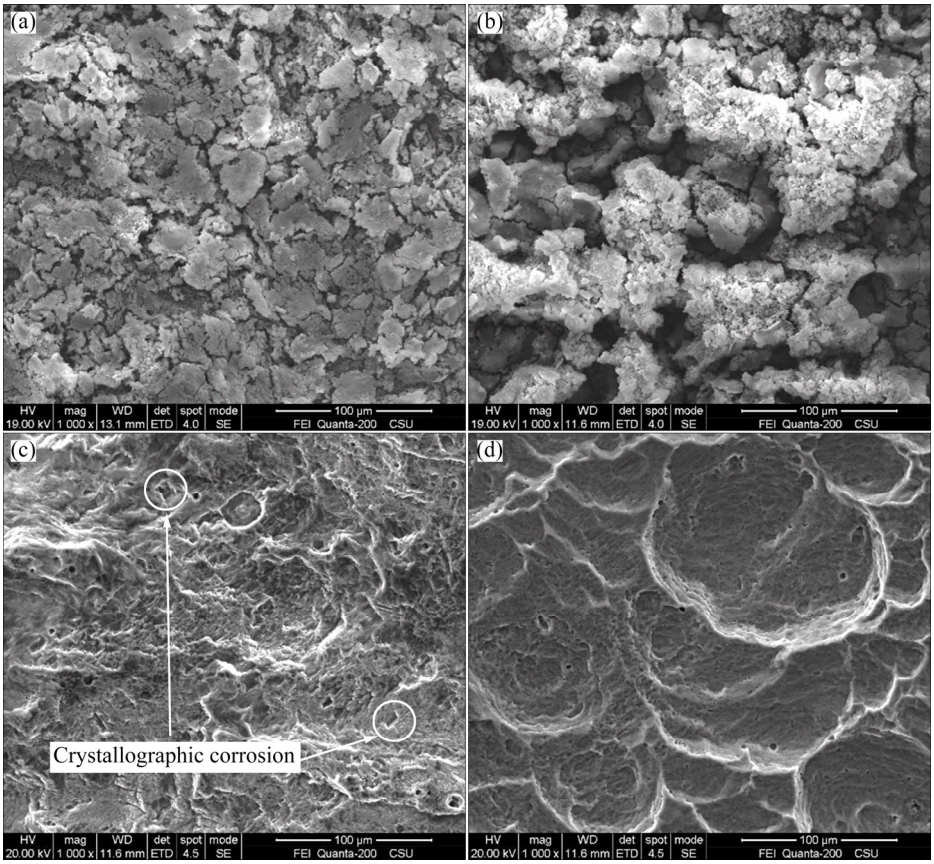

Fig. 4 Corrosion morphologies of Al alloys after immersion in 4 mol/L NaOH solution for 150 min with (a, b) and without (c, d) corrosion products: (a, c) Alloy 1; (b, d) Alloy 2

porous and loose, while the corrosion product on the surface of Alloy 2 is piled and thick. This reveals that Alloy 2 has a relatively compact protective film to hinder the corrosion reaction on the Al matrix. By removing the corrosion product, two alloys show general corrosion morphology. Especially, crystallographic corrosion with {100} facets exists in Alloy 1, as shown in Fig. 4(c). The geometric facet corrosion can be explained by the fact that the attack occurs according to well-defined crystallographic directions, which is in agreement with other authors [35]. In Fig. 4(d), Alloy 2 shows flat general corrosion morphology. This phenomenon is attributed to the homogeneous distribution of second phases and elements in Alloy 2. As seen in Fig. 1 and Fig. 2, no coarse second phase precipitates at the grain boundary in Alloy 2 and the second phases rich in Mg and Sn elements are dispersed homogeneously in the grain. This leads to restrained grain boundary corrosion [37]. Moreover, the annealing process also decreases the dislocation density, stress, and distortion energy at the grain boundary. The grain boundary in the thermodynamic equilibrium state is not necessarily the weak corrosion area [38]. Meanwhile, the second phases generally act as the cathode center during the corrosion process. Thus, the corrosion starts around the second phase in the grain and develops to general corrosion in Alloy 2, which is in agreement with other authors [21].

The corrosion behavior of Al alloys is related to the microstructure features. Alloy 2 expresses better corrosion resistance than Alloy 1 for the following reasons. Firstly, the solid solution of element Ga in the Al matrix can suppress the hydrogen evolution rate and decrease the self-corrosion rate of aluminum due to its high hydrogen evolution over-potential. Secondly, the addition of element Ga decreases the amount and size of the second phases, showing a relatively homogeneous microstructure compared with Alloy 1, as shown in Fig. 1. The effect of micro-galvanic corrosion in Alloy 2 is inhibited, resulting in the enhancement of the corrosion resistance. Thirdly, the addition of Ga leads to the homogeneous distribution of element Hg in the Al matrix and

second phases, as seen in Table 2 and Fig. 2(b). Hg has a positive standard electrode potential (0.79 V vs SCE) and acts as a strong cathode in Al alloys. Hg also has high hydrogen evolution over-potential as Ga. The homogeneous distribution of element Hg in Alloy 2 further hinders the micro-galvanic corrosion and suppresses the hydrogen evolution of the alloy. However, it is reported that the addition of gallium in Al−Mg−Sn-based alloy results in severe intergranular corrosion of the alloy anode [21]. As a result, a synergistic effect is found between Hg and Ga in Al−Mg−Sn alloy.

3.4 Electrochemical impedance spectroscopy (EIS) results

Figure 5 shows the EIS of Alloy 1 and Alloy 2 at OCP. The EIS of Alloy 2 in 4 mol/L NaOH solutions is characterized by a high-frequency (HF) capacitive loop and an unobvious low-frequency (LF) capacitive loop. As for Alloy 1, the EIS plot reveals a middle-frequency (MF) inductive loop and two capacitive loops at HF and LF, respectively.

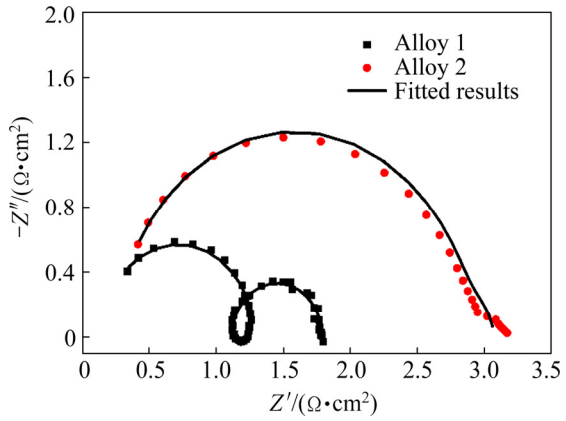

Fig. 5 EIS curves and fitted results of Alloy 1 and Alloy 2 in 4 mol/L NaOH solution

The equivalent circuits in Fig. 6 for simulating the process are used, and the fitted values obtained via ZVIEW software are listed in Table 4. R_s represents the solution resistance and R_t is the charge-transfer resistance. The constant phase angle element (CPE) is adopted to describe the non-ideal capacitive behavior, which is caused by the microscopic roughness of the electrode surface [39]. The capacitive semicircle at high frequencies is attributed to the redox reaction: $Al \rightarrow Al^{+}+e$, where the equivalent component consists of a charge transfer resistance (R_t) in parallel with a double-layer capacitance (CPE_{dl}) [4]. It can be assumed that this is the rate-determining step in the charge transfer process and R_t is directly proportional to the corrosion resistance of the working electrode. The R_f in parallel with CPE_f is used to illustrate the low-frequency capacitive loop associated with the formation of the $Al(OH)_3$ film on the electrode surface [40]. The inductive loop in Alloy 1 is described via the parallel connection of R_l and L, which can be attributed to the obstruction of the corrosion product film and the incubation of localized corrosion, as confirmed by the localized crystallographic corrosion morphology shown in Fig. 4(c).

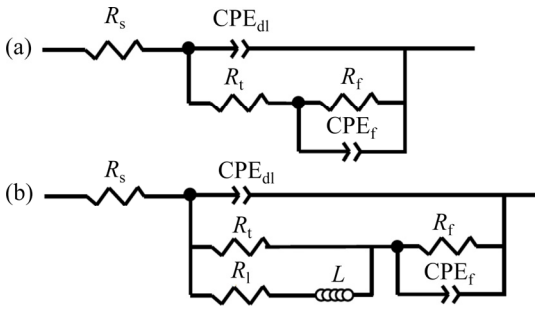

Fig. 6 Equivalent circuits used for fitting EIS of Alloy 2 (a) and Alloy 1 (b)

Table 4 EIS simulated values of different anodes

Parameter	Alloy 1	Alloy 2
$R_s/(\Omega\cdot cm^2)$	0.15	0.26
$R_t/(\Omega\cdot cm^2)$	1.14	2.65
$Y_{dl}/(\Omega^{-1}\cdot cm^{-1}\cdot s^n)$	1.91×10^{-5}	6.71×10^{-5}
n_{dl}	1	0.97
$R_f/(\Omega\cdot cm^2)$	0.68	0.17
$Y_f/(\Omega^{-1}\cdot cm^{-1}\cdot s^n)$	4.42×10^{-2}	1.70×10^{-2}
n_f	1	0.97
$R_l/(\Omega\cdot cm^2)$	6.18	–
$L/(mH\cdot cm^2)$	4.66×10^{-3}	–
$R_p/(\Omega\cdot cm^2)$	1.79	3.08

According to Table 4, R_t reduces in the following order: Alloy 2>Alloy 1. The addition of Ga greatly enhances the capacitive semicircle, indicating that R_t markedly increases, which is beneficial for the performance of Al−air batteries. In addition, the polarization resistance (R_p) can be calculated via Eqs. (8) and (9) according to their equivalent circuits. The reciprocal polarization

resistance is proportional to the corrosion rate. According to Table 4, Alloy 2 with larger polarization resistance has better corrosion resistance than the Alloy 1 at OCP. The results are consistent with the result of polarization and mass loss measurements:

$$R_p=R_s+R_t+R_f \quad (8)$$

$$R_p=R_s+R_tR_L/(R_t+R_L)+R_f \quad (9)$$

3.5 Battery performance and discharge morphology

The discharge behavior of the Al−air battery with different anodes and current densities are shown in Fig. 7. The related discharge parameters are given in Table 5. Compared with Alloy 1, the specific capacity of Alloy 2 increases by 47.7% and 13.7% at 10 and 20 mA/cm^2, respectively, indicating better battery performance.

According to Fig. 8, the corrosion film on the surface of Alloy 1 is mostly compact with unbroken hydrogen bubbles, while more broken hydrogen bubbles can be seen in Alloy 2, due to the hydrogen evolution reaction given in Eq. (6). The broken hydrogen bubbles in Alloy 2 can make the corrosion film easier to degrade in solutions and

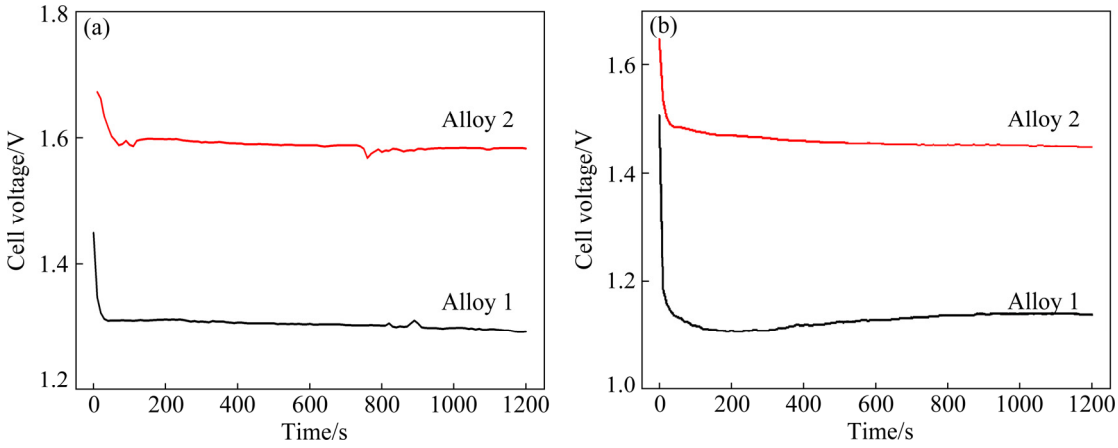

Fig. 7 Discharge curves of Alloy 1 and Alloy 2 at different current densities in 4 mol/L NaOH solution: (a) 10 mA/cm^2; (b) 20 mA/cm^2

Table 5 Discharge performances of different alloys in alkaline solution

Sample	Solution	Discharge voltage/V		Current efficiency/%		Specific capacity/(mA·h·g^{-1})	
		10 mA/cm^2	20 mA/cm^2	10 mA/cm^2	20 mA/cm^2	10 mA/cm^2	20 mA/cm^2
Alloy 1	4 mol/L NaOH	1.31	1.13	15.9	29.1	248.3	879.9
Alloy 2		1.59	1.46	30.4	33.1	474.9	1019.2
Al−0.5Mg−0.1Sn−0.02In [41]		−	1.22	−	4.6	−	136.8
Al−0.5Mg−0.1Sn−0.02Ga [41]		−	1.19	−	18.4	−	547.1
Al−0.5Mg−0.1Sn [21]		1.55	1.45	50.5	70.0	1562.9	2080.9
Al−0.5Mg−0.1Sn−0.05In [21]		1.59	1.52	61.9	74.1	1840.9	2203.0
Al−0.5Mg−0.1Sn−0.05Bi [21]		1.57	1.49	39.2	56.5	1165.8	1680.2
Al−0.5Mg−0.1Sn−0.05Ga [21,42]		1.63−1.73	1.55−1.65	16.8−50.4	25.2−74.0	500−1500	750−2200
Al−0.06Sb [43]	4 mol/L KOH	1.54	1.40	77.8	~87.3	2317	~2600
Al−0.36Sb [43]		1.57	1.42	70.0	~84.1	2083	~2500
Al−0.5Mg [15]	6 mol/L NaOH + 0.05 mol/L Na_2SnO_3		~1.60		82.5		2455.2
Al−8Mg [15]			~1.60		32.0		933.7

inspire the discharge activity. Although the hydrogen evolution reaction on the surface of the alloy decreases the anodic efficiency to some degree, the chunk effect induced by large current density during discharge is the main reason for the anodic efficiency loss [44]. Some anode materials with a high hydrogen evolution reaction rate can show good anodic efficiency because of the less chunk effect [44]. Alloy 2 has refined second phases and homogenous microstructure (as seen in Fig. 1 and Fig. 2), which implies decreased chunk effect and generates high anodic efficiency. The corrosion morphologies of Alloy 1 and Alloy 2 discharged at the current density of 20 mA/cm^2 in 4 mol/L NaOH solution after removing the discharge products are shown in Fig. 9. As can be

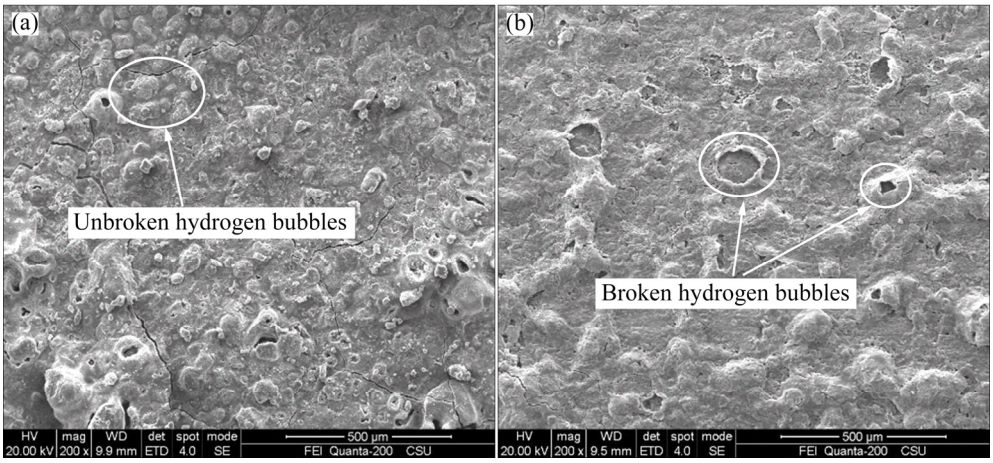

Fig. 8 Corrosion morphologies of alloys after discharge at current density of 20 mA/cm^2 for 20 min in 4 mol/L NaOH solution: (a) Alloy 1; (b) Alloy 2

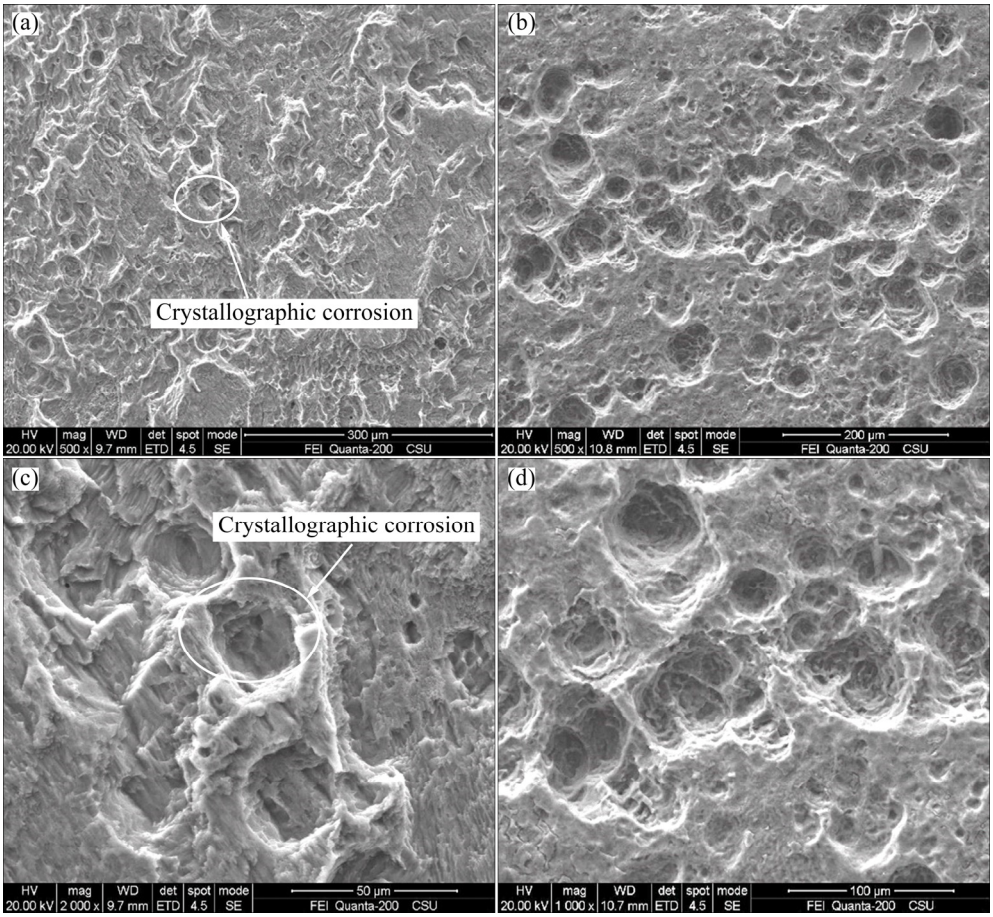

Fig. 9 Surface morphologies of alloys discharged at current density of 20 mA/cm^2 for 20 min in 4 mol/L NaOH solution after removing discharge products: (a, c) Alloy 1; (b, d) Alloy 2

seen in the enlarged image, the corrosion of the aluminum matrix is flaky and along a specific direction. The presence of some geometric facets can be explained by the fact that the corrosion occurs probably along with the well-defined crystallographic directions of {100} facets [35]. Apparently, Alloy 2 has more homogeneous anodic dissolution than Alloy 1, indicating its higher electrochemical activity.

The reasons for Alloy 2 to exhibit better battery performance can be as follows. Firstly, the addition of gallium elements can reduce oxide film resistance [19]. The EIS result in Table 4 shows that Alloy 2 has a lower R_f value than Alloy 1. During discharge, Ga element can act as single or multiple atomic states into the defects or cracks of the oxidation film and separate the surface film and accelerate the dissolution of aluminum [45]. Secondly, the addition of gallium improves the homogeneous distribution of the second phase (as seen in Fig. 1). The uniform microstructure in Alloy 2 accelerates uniform dissolution during discharge, as seen in Fig. 9(d). However, in Alloy 1, crystallographic corrosion morphology occurs during discharge (Fig. 9(c)). It is the same as the corrosion morphology after immersion in 4 mol/L NaOH solution (Fig. 4(c)). This selective corrosion results in local dissolution during discharge [41] and lowers the discharge activity of Alloy 1. Thirdly, the addition of element Ga in aluminum anode alloys can produce a synergistic effect with element Hg to facilitate the stripping of the corrosion products. Sn, Hg and Ga elements with a low melting point can dissolve and re-deposit on the aluminum surface, stripping the corrosion products and sustaining the alloy in the highly active state [45,46]. Thus, Alloy 2 exhibits higher electrochemical activity than the Alloy 1.

4 Conclusions

(1) The addition of 0.01 wt.% Ga in Al−0.4Mg−0.05Sn−0.03Hg alloy refines the second phases and promotes homogeneous microstructure. Mg and Sn elements enrich in the second phases, and the low-melting-point elements, Hg and Ga, distribute uniformly in Al−0.4Mg−0.05Sn−0.03Hg−0.01Ga.

(2) The refined second phases and the homogeneous microstructure in Al−0.4Mg−0.05Sn−0.03Hg−0.01Ga alloy restrain the local crystallographic corrosion and chunk effect, leading to uniform discharge dissolution and increased corrosion resistance and electrochemical performance. With the addition of Ga, the corrosion current density of Al−0.4Mg−0.05Sn−0.03Hg−0.01Ga alloy decreases significantly from 14.12 to 6.05 mA/cm^2 and the mass loss rate decreases from 39.06 to 2.48 mg·cm^{-2}·h^{-1}.

(3) When discharging at the current density of 20 mA/cm^2, the discharge voltage, current efficiency, and specific capacity of a single Al−air battery with Al−0.4Mg−0.05Sn−0.03Hg−0.01Ga anode are 1.46 V, 33.1% and 1019.2 A·h·kg^{-1}, respectively.

Acknowledgments

This work is supported by the Equipment Pre-research Laboratory Foundation in Central South University, China (No. 6142912200104).

References

[1] MA Jing-ling, WEN Jiu-ba, GAO Jun-wei, LI Quan-an. Performance of Al−0.5Mg−0.02Ga−0.1Sn−0.5Mn as anode for Al–air battery in NaCl solutions [J]. Journal of Power Sources, 2014, 253: 419−423.

[2] GOEL P, DOBHAL D, SHARMA R C. Aluminum–air batteries: A viability review [J]. Journal of Energy Storage, 2020, 28: 101287.

[3] ILYUKHINA A V, KLEYMENOV B V, ZHUK A Z. Development and study of aluminum−air electrochemical generator and its main components [J]. Journal of Power Sources, 2017, 342: 741−749.

[4] FAN Liang, LU Hui-min, LENG Jing. Performance of fine structured aluminum anodes in neutral and alkaline electrolytes for Al−air batteries [J]. Electrochimica Acta, 2015, 165: 22−28.

[5] REN Jian-ming, MA Jian-bo, ZHANG Jiao, FU Chao-peng, SUN Bao-de. Electrochemical performance of pure Al, Al–Sn, Al–Mg and Al–Mg–Sn anodes for Al−air batteries [J]. Journal of Alloys and Compounds, 2019, 808: 151708.

[6] ZHANG Peng-ju, LIU Xuan, XUE Ji-lai, JIANG Kai-xi. The role of microstructural evolution in improving energy conversion of Al-based anodes for metal−air batteries [J]. Journal of Power Sources, 2020, 451: 227806.

[7] HAN Xiao-yu, QU You-peng, DONG Yue, ZHAO Jia-yi, JIA Li-ming, YU Yan-ling, ZHANG Peng, LI Da, REN Nan-qi, FENG Yu-jie. Microbial electrolysis cell powered by an aluminum-air battery for hydrogen generation, in-situ coagulant production and wastewater treatment [J]. International Journal of Hydrogen Energy, 2018, 43(16): 7764−7772.

[8] SUN Ze-gao, LU Hui-min. Performance of Al−0.5In as anode

for Al−air battery in inhibited alkaline solutions [J]. Journal of the Electrochemical Society A, 2015, 162(8): 1617−1623.

[9] YANG Han-xue, LI Xiao-hui, WANG Yi-jun, GAO Li-xin, LI Jin, ZHANG Da-quan, LIN Tong. Excellent performance of aluminium anode based on dithiothreitol additives for alkaline aluminium/air batteries [J]. Journal of Power Sources, 2020, 452: 227785.

[10] JIANG Hao, YU Sha, LI Wen-zhang, YANG Ya-hui, YANG Li-shan, ZHANG Ze-jie. Inhibition effect and mechanism of inorganic-organic hybrid additives on three-dimension porous aluminum foam in alkaline Al−air battery [J]. Journal of Power Sources, 2020, 448: 227460.

[11] LI Li, LIU Hui, YAN Yang, ZHU Hua-long, FANG Hong-jie, LUO Xi-er, DAI Yi-long, YU Kun. Effects of alloying elements on the electrochemical behaviors of Al−Mg−Ga−In based anode alloys [J]. International Journal of Hydrogen Energy, 2019, 44(23): 12073−12084.

[12] LI Jia-run, CHEN Zhuo-yuan, JING Jiang-ping, HOU Jian. Electrochemical behavior of Mg−Al−Zn−Ga−In alloy as the anode for seawater-activated battery [J]. Journal of Materials Science & Technology, 2020, 41: 33−42.

[13] PARK I, CHOI S, KIM J. Aluminum anode for aluminum−air battery. Part II: Influence of In addition on the electrochemical characteristics of Al−Zn alloy in alkaline solution [J]. Journal of Power Sources, 2017, 357: 47−55.

[14] AFSHARI M, ABBASI R, SOVIZI M R. Evaluation of nanometer-sized zirconium oxide incorporated Al−Mg−Ga−Sn alloy as anode for alkaline aluminum batteries [J]. Transactions of Nonferrous Metals Society of China, 2020, 30(1): 90−98.

[15] GAO Jian-xin, FAN He-fei, WANG Er-dong, SONG Yu-jiang, SUN Gong-quan. Exploring the effect of magnesium content on the electrochemical performance of aluminum anodes in alkaline batteries [J]. Electrochimica Acta, 2020, 353: 136497.

[16] ZHANG Chun, WANG Ri-chu, FENG Yan, QIU Ke, PENG Chao-qun. Effects of alloying elements on electrochemical performance of aluminum anodes [J]. Journal of Central South University (Science and Technology), 2012, 43(1): 81−86. (in Chinese).

[17] MOKHTAR M, TALIB M Z M, MAJLAN E H, TASIRIN S M, RAMLI W M F W, DAUD W R W, SAHARI J. Recent developments in materials for aluminum–air batteries: A review [J]. Journal of Industrial and Engineering Chemistry, 2015, 32: 1−20.

[18] TUCK C D S, HUNTER J A, SCAMANS G M. The electrochemical behavior of Al−Ga alloys in alkaline and neutral electrolytes [J]. Journal of the Electrochemical Society, 1987, 134: 2970−2981.

[19] SHAYEB H A E, WAHAB F M A E, ABEDIN S Z E. Effect of gallium ions on the electrochemical behaviour of Al, Al−Sn, Al−Zn and Al−Zn-Sn alloys in chloride solutions [J]. Corrosion Science, 2001, 43: 643−654.

[20] WANG Nai-guang, WANG Ri-chu, PENG Chao-qun, FENG Yan, ZHANG Chun, ZHANG Pei-jia. Influence of alloying elements on electrochemical behavior and microstructure of Al anode materials [J]. Journal of Central South University (Science and Technology), 2010, 41(2): 495−500. (in Chinese).

[21] WU Zi-bin, ZHANG Hai-tao, GUO Cheng, ZOU Jing, QIN Ke, BAN Chun-yan, NAGAUMI H. Effects of indium, gallium, or bismuth additions on the discharge behavior of Al−Mg−Sn-based alloy for Al−air battery anodes in NaOH electrolytes [J]. Journal of Solid State Electrochemistry, 2019, 23(8): 2483−2491.

[22] ZHOU Sheng-gang, TIAN Chang, ALZOABI S, XU Yang, JIAO Zeng-kai, LUO Kai-liang, PENG Bin, ZHANG Cong, SANTOS N, CAO Yong. Performance of an Al−0.08Sn−0.08Ga−*x*Mg alloy as an anode for Al–air batteries in alkaline electrolytes [J]. Journal of Materials Science, 2020, 55(25): 11477−11488.

[23] EL ABEDIN S Z, SALEH A O. Characterization of some aluminium alloys for application as anodes in alkaline batteries [J]. Journal of Applied Electrochemistry, 2004, 34(3): 331−335.

[24] ZHANG Jin-suo, KLASKY M, LETELLIER B C. The aluminum chemistry and corrosion in alkaline solutions [J]. Journal of Nuclear Materials, 2009, 384(2): 175−189.

[25] WANG Qin, MIAO He, XUE Ye-jian, SUN Shan-shan, LI Shi-hua, LIU Zhao-ping. Performances of an Al–0.15Bi−0.15Pb−0.035Ga alloy as an anode for Al–air batteries in neutral and alkaline electrolytes [J]. RSC Advances, 2017, 7: 25838−25847.

[26] NESTORIDI M, PLETCHER D, WOOD R J K, WANG S, JONES R L, STOKES K R, WILCOCK I. The study of aluminium anodes for high power density Al/air batteries with brine electrolytes [J]. Journal of Power Sources, 2008, 178(1): 445−455.

[27] CHO Y, PARK I, LEE H, KIM J. Aluminum anode for aluminum–air battery. Part I: Influence of aluminum purity [J]. Journal of Power Sources, 2015, 277: 370−378.

[28] XIONG Han-qing, YIN Xiang, YAN Yang, DAI Yi-long, FAN Su-feng, QIAO Xue-yan, YU Kun. Corrosion and discharge behaviors of Al−Mg−Sn−Ga−In in different solutions [J]. Journal of Materials Engineering and Performance, 2016, 25(8): 3456−3464.

[29] FENG Yan, LEI Ge, HE Yu-qing, WANG Ri-chu, WANG Xiao-feng. Discharge performance of Mg−Al−Pb−La anode for Mg−air battery [J]. Transactions of Nonferrous Metals Society of China, 2018, 28(11): 2274−2286.

[30] FENG Yan, WANG Ri-chu, PENG Chao-qun. Magnesium alloy and aluminum alloy anode materials [M]. Changsha: Central South University Press, 2015.

[31] PLEVACHUK Y, SKLYARCHUK V, ECKERT S, GERBETH G, NOVAKOVIC R. Thermophysical properties of the liquid Ga−In−Sn eutectic alloy [J]. Journal of Chemical & Engineering Data, 2014, 59(3): 757−763.

[32] MOKHTAR M, TALIB M Z M, MAJLAN E H, TASIRIN S M, RAMLI W M F W, DAUD W R W, SAHARI J. Recent developments in materials for aluminum–air batteries: A review [J]. Journal of Industrial and Engineering Chemistry, 2015, 32: 1−20.

[33] XU Shuo, ZHAO Xi, LIU Jing. Liquid metal activated aluminum-water reaction for direct hydrogen generation at room temperature [J]. Renewable & Sustainable Energy Reviews, 2018, 92: 17−37.

[34] FENG Yan, LI Xiao-gen, WANG Ri-chu, PENG Chao-qun, LIU Li. Influence of cerium on microstructures and

electrochemical properties of Al−Mg−Sn−Hg anode materials for seawater battery [J]. Journal of Rare Earths, 2015, 33(9): 1010−1016.
[35] LIU Jian-cai, ZHANG Xin-ming, CHEN Ming-an, LI Li, ZHU Bing, TANG Jian-guo, LIU Sheng-dan. DFT study on surface properties and dissolution trends of Al(100) surfaces doped with Zn, Ga, In, Sn and Pb [J]. Applied Surface Science, 2011, 257(9): 4004−4009.
[36] MA Jing-ling, WEN Jiu-ba, GAO Jun-wei, LI Quan-an. Performance of Al−1Mg−1Zn−0.1Ga−0.1Sn as anode for Al-air battery [J]. Electrochimica Acta, 2014, 129: 69−75.
[37] LI Jia-run, ZHANG Bin-bin, WEI Qin-yi, WANG Ning, HOU Bao-rong. Electrochemical behavior of Mg−Al−Zn−In alloy as anode materials in 3.5 wt.% NaCl solution [J]. Electrochimica Acta, 2017, 238: 156−167.
[38] WANG Wen-hui, WU Hong-liu, SUN Yu, YAN Jun, ZHANG Lei, ZHANG Shao-xiang, NI Jia-hua, SONG Yang, ZHANG Xiao-nong. Local intragranular misorientation accelerates corrosion in biodegradable Mg [J]. Acta Biomaterialia, 2020, 101: 575−585.
[39] MACDONALD M U, REAL S, MACDONALD D D. Applications of Kramers−Kronig transforms in the analysis of electrochemical impedance date-Ⅲ [J]. Electrochimica Acta, 1990, 35(10): 1559−1566.
[40] PARDO A, MERINO M C, COY A E, VIEJO F, ARRABAL R, FELIÚ S. Influence of microstructure and composition on the corrosion behaviour of Mg/Al alloys in chloride media [J]. Electrochimica Acta, 2008, 53(27): 7890−7902.
[41] MA Jing-ling, WEN Jiu-ba, REN Feng-zhang, WANG Guang-xin, XIONG Yi. Electrochemical performance of Al−Mg−Sn based alloys as anode for Al−air battery [J]. Journal of the Electrochemical Society A, 2016, 163(8): 1759−1764.
[42] WU Zi-bin, ZHANG Hai-tao, ZOU Jing, SHEN Xiao-dong, QIN Ke, BAN Chun-yan, CUI Jian-zhong, NAGAUMI Hiromi. Enhancement of the discharge performance of Al−0.5Mg−0.1Sn−0.05Ga (wt.%) anode for Al−air battery by directional solidification technique and subsequent rolling process [J]. Journal of Alloys and Compounds, 2020, 827: 154272.
[43] LIU Xuan, ZHANG Peng-ju, XUE Ji-lai. The role of micro−naoscale AlSb precipitates in improving the discharge performance of Al−Sb alloy anodes for Al−air batteries [J]. Journal of Power Sources, 2019, 425: 186−194.
[44] DENG Min, WANG Lin-qian, HÖCHE D, LAMAKA S V, SNIHIROVA D, VAGHEFINAZARI B, ZHELUDKEVICH M L. Clarifying the decisive factors for utilization efficiency of Mg anodes for primary aqueous batteries [J]. Journal of Power Sources, 2019, 441: 227201.
[45] LI Zhen-ya, YI Ling, LIU Zhi-hui, YANG Lin, SU Jing-xin, CHEN Yan-ying. The activation mechanism of Al alloys with tin and gallium in alkaline electrolytes [J]. J Electrochem, 2001, 7(3): 316−320.
[46] WU Jun-liang, WANG Ri-chu, FENG Yan, PENG Chao-qun. Effect of hot rolling on the microstructure and discharge properties of Mg−1.6 wt.%Hg−2wt.%Ga alloy anodes [J]. Journal of Alloys and Compounds, 2018, 765: 736−746.

合金元素 Ga 对铝空气电池阳极 Al−0.4Mg−0.05Sn−0.03Hg 合金显微组织和电化学性能的影响

庄泽航[1]，冯 艳[1,2]，彭超群[1,2]，杨柳忠[1]，王 檬[1]

1. 中南大学 材料科学与工程学院，长沙 410083；
2. 中南大学 电子封装与先进功能材料重点实验室，长沙 410083

摘 要：采用动电位极化法、电化学阻抗谱法和恒电流放电法研究添加 0.01%Ga(质量分数)对 Al−0.4Mg−0.05Sn−0.03Hg 阳极的显微组织和在 NaOH 溶液中的电化学性能的影响。结果表明，Ga 的添加增强 Al−Mg−Sn−Hg 阳极的耐蚀性和放电活性，这得益于 Ga 的加入能细化 Al−Mg−Sn−Hg 阳极的第二相，使显微组织更加均匀，从而抑制局部腐蚀和块效应。与 Al−Mg−Sn−Hg 阳极相比，Al−Mg−Sn−Hg−Ga 阳极的腐蚀电流密度降低 57%，质量损失率降低 93%。在 20 mA/cm^2 放电电流流密度下，以 Al−0.4Mg−0.05Sn−0.03Hg−0.01Ga 为阳极的单个铝空气电池的放电电压、电流效率和放电容量分别为 1.46 V，33.1%和 1019.2 A·h·kg^{-1}。此外，还讨论 Ga 在 Al−Mg−Sn−Hg− Ga 阳极材料上的活化机理。

关键词：铝合金；电化学；腐蚀；铝空气电池

(Edited by Bing YANG)